GRAINE project: The first balloon-borne, emulsion gamma-ray telescope experiment

Takahashi, Satoru ; Aoki, Shigeki ; Kamada, Keiki ; Mizutani, Saki ; Nakagawa, Ryo ; Ozaki, Keita ; Rokujo, Hiroki

GRAINE project: The first balloon-borne, emulsion gamma-ray telescope experiment

Satoru Takahashi[1,*], Shigeki Aoki[1], Keiki Kamada[1,†], Saki Mizutani[1,†], Ryo Nakagawa[1,†], Keita Ozaki[1], and Hiroki Rokujo[1,‡]

[1]*Kobe University, Nada, Kobe 657-8501, Japan*
*E-mail: satoru@radix.h.kobe-u.ac.jp

. . . .
The GRAINE project (Gamma-Ray Astro-Imager with Nuclear Emulsion) has been developed for the observation of cosmic γ-rays in the energy range 10 MeV–100 GeV with a precise (0.08° at 1–2 GeV), polarization-sensitive, large-aperture-area ($\sim$10 m^2) emulsion telescope by repeated long-duration balloon flights. In 2011, the first balloon-borne experiment was successfully performed with a 12.5×10 cm^2 aperture area and 4.6 hour flight duration for a feasibility and performance test. Systematic detection, energy reconstruction, and timestamping of γ-ray events were performed across the whole area of the emulsion film, up to 45° incident zenith angle, down to 50 MeV γ-ray energy, with 97% detection reliability, 0.2 sec timestamp accuracy, and 98% timestamp reliability. A γ-ray data checking and calibration method was created using the γ-rays produced in the converter. We measured the atmospheric γ-ray flux in the energy range 50–300 MeV and obtained a first understanding of the cosmic γ-ray background. By combining the attitude data, we established a procedure for determining the γ-ray arrival direction in celestial coordinates. The first flight of the balloon-borne emulsion telescope confirmed its potential as a high-performance cosmic γ-ray detector.
. . . .

Subject Index   H22

1. Introduction

The observation of high-energy cosmic γ-rays can provide direct information on high-energy phenomena in the universe. Currently, AGILE [1] and Fermi-LAT [2] are observing the γ-ray sky. Fermi-LAT has detected 1873 γ-ray sources [3] and is greatly advancing the field of γ-ray observations. As a result of these observations, a much greater understanding of high-energy phenomena has been achieved.

However, past and current γ-ray observations have significant limitations. The angular resolution is orders of magnitude poorer than other wavelength observations, in spite of its critical importance for astronomical observations. The polarization of cosmic γ-rays has never been measured in spite of its significance. The improvement of angular resolution and polarization sensitivity are aims of the next generation of cosmic γ-ray experiments.

The interaction of high-energy γ-rays with matter is dominated by the electron pair creation process. Observing electron pairs can provide information on the arrival direction, energy, arrival timing,

---

[†]Graduated.

[‡]Present address: Nagoya University, Nagoya 464-8602, Japan

and polarization of the γ-rays. The suppression of multiple Coulomb scattering and precise tracking provide us with an accurate determination of the γ-ray direction of travel and sensitivity to γ-ray polarization.

A nuclear emulsion is a powerful tracking device that can record the 3D trajectory of a charged particle within $1\,\mu$m accuracy. Several prominent observations have been performed with nuclear emulsion, e.g., the discovery of the π meson [4], the discovery of a charmed particle [5], the first observation of tau-neutrino interactions [6], and observation of the $\nu_\mu \to \nu_\tau$ appearance [7–10]. By detecting the beginning of an electron pair created by γ-rays using an emulsion film that is thin ($\sim 2.0 \times 10^{-3}$ radiation lengths) and precise ($\sim$submilliradian), the γ-ray direction can be precisely determined and it is sensitive to the γ-ray linear polarization.

In recent years, significant progress in emulsion techniques (emulsionics) has been achieved. The emulsion film is a highly precise, quite uniform, refreshable, and mass-producible tracking device [11]. Emulsion scanning is automated and the achievable scanning speed is increasing exponentially [12–16]. Multi-stage shifter techniques allow a track timing resolution of <1 sec with high reliability and high efficiency for large-scale and inaccessible emulsion experiments [17]. In 2004 a balloon-borne experiment with the latest emulsionics was performed for the observation of primary electrons [18]. After that experiment, the potential for a high-performance γ-ray telescope with a nuclear emulsion target became apparent. The latest emulsionic techniques allow the possibility of novel cosmic γ-ray observation with nuclear emulsions.

We are conducting a project involving 10 MeV–100 GeV cosmic γ-ray observations with a precise (0.08° at 1–2 GeV), polarization-sensitive, large-aperture-area ($\sim 10\,\text{m}^2$) emulsion telescope by repeated long-duration balloon flights [19–21]. We call this project GRAINE (Gamma-Ray Astro-Imager with Nuclear Emulsion).

To demonstrate the feasibility and performance of the emulsion γ-ray telescope, various test experiments have been performed on the ground. The angular resolution was demonstrated in exposure tests with an accelerator γ-ray beam (inverse Compton scattering γ-ray beam) at LEPS/SPring-8 (max. 2.4 GeV) in 2004 and at UVSOR (max. 47 MeV) in 2007 (Fig. 27) [22]. The γ-ray polarization sensitivity was also checked using an emulsion chamber exposed at LEPS/SPring-8 [22,23]. The γ-ray event detectability was demonstrated in a cosmic ray exposure test at Norikura Observatory (2770 m a.s.l.) in 2007, using atmospheric γ-rays [22].

In 2011, the first balloon-borne emulsion γ-ray telescope experiment was performed to demonstrate the feasibility and performance of this detector in a balloon flight. In this paper, the 2011 balloon experiment and the flight data analysis are described.

2. Emulsion chamber

Figure 1 shows the schematic structure of the emulsion chamber used in the 2011 balloon experiment. The emulsion chamber with a $12.5 \times 10\,\text{cm}^2$ aperture area consists of a converter, a timestamper, and a calorimeter. The converter plays the role of a target and a detector for the incident γ-rays. A precise measurement of the γ-ray incidence angle and the azimuth angle measurement of the electron pair plane for polarization measurement are performed around the conversion point. γ-ray energy events below $\sim$GeV are reconstructed by measuring the momentum of electron pairs using multiple Coulomb scattering. Multiple Coulomb scattering can be measured with emulsion films. The deviations of scattering angle and position are inversely proportional to the particle momentum. A measurement accuracy within 10% can be achieved. The bottom part of the converter functions
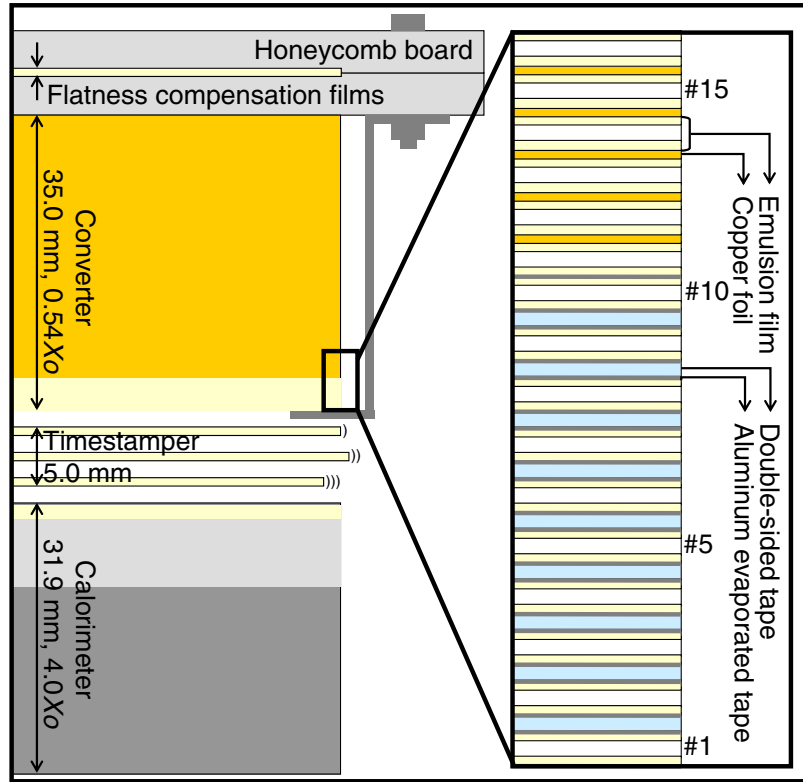
Fig. 1. Schematic structure of the emulsion chamber (side view). The chamber consisted of the converter, timestamper, and calorimeter. Converter films were numbered from bottom to top.

as the interface to the timestamper. The timestamper provides an accurate assignment of the time of arrival (or timestamp) information for all tracks, and hence for γ-ray events observed in the emulsion chamber. The timestamping of γ-ray events is essential for conversion of their incident directions into celestial sphere coordinates with attitude monitor data. The calorimeter enables energy measurement of γ-rays above $\sim$GeV with multiple Coulomb scattering and/or with electromagnetic showers. The emulsion films were held by mechanical supports and adhesive tape.

The converter consisted of a stack of 102 emulsion films and 91 copper foils (50 μm thickness). The emulsion films were OPERA films [11], except for four films located at the top part of the converter. The OPERA films were 293 μm thick, consisting of 44 μm thick emulsion layers coated on both sides of a 205 μm thick TAC (cellulose triacetate) base. The emulsion layers consisted of 200 nm silver bromide crystals dispersed in gelatine. The silver bromide crystals are sensitive to charged particles passing through them. The charged particle trajectory can be recognized as a grain line using an optical microscope after development. The intrinsic positional accuracy at the center of each grain was 60 nm. The four films located at the top part of the converter were 170 μm thick high-sensitivity emulsion gel films, consisting of 50 μm thick emulsion layers coated on both sides of a 70 μm thick PS (polystyrene) base. The high-sensitivity emulsion gel had a high grain density due to the silver bromide crystal density being enriched by reducing the amount of gelatine in the emulsion gel to a quarter of that in the OPERA-type emulsion gel [26]. This is the first practical use of high-sensitivity emulsion gel films. The ten films at the bottom part of the converter functioned as a bottom plate to hold the converter films on aluminum honeycomb boards, constructed by

putting emulsion films coated with 25 μm thick aluminum evaporated tapes[1] on 47 μm thick double-sided tapes[2]. An aluminum evaporated tape coating was used to avoid warping of the emulsion film during rapid drying. The total thickness and radiation length (X_o) of the converter were 35.0 mm and 0.54 X_o, corresponding to a 0.34 conversion efficiency. At the upper part of the converter, two OPERA films were installed for flatness compensation. The flatness was mechanically compensated for by placing the films between honeycomb boards. The total thickness above the top of the converter was 1.46 g/cm^2 (1.20 g/cm^2 honeycomb boards, 0.13 g/cm^2 insulating foam, 0.10 g/cm^2 flatness compensation films, and 0.03 g/cm^2 film packing).

The timestamper consisted of a multi-stage shifter, namely, a series of emulsion films that are shifted with individual cycles. The independent position relations of the emulsion films in the time-stamper are created for each timing from a combination of individual cycles. In the analysis, by combining the relative positions of a track between films, the incident timing can be reconstructed with an accuracy of less than a second. A flight model of the multi-stage shifter was co-developed with Mitaka Kohki Co., Ltd. based on the invention [17]. The multi-stage shifter consisted of three stages, with two films in the 1st stage, two films in the 2nd stage and four films in the 3rd stage. OPERA films were used throughout, except for the 3rd film in the 3rd stage, which was equipped with a high-sensitivity emulsion gel film. The multi-stage shifter was continuously operated from 22 km altitude to system shutdown. The 1st stage was stepped by 410 μm every 1000 sec. The 2nd stage was stepped by 300 μm every 50 sec and was cycled over 20 steps every 1000 sec. The 3rd stage was continuously reciprocated over 2500 μm at 50 μm/sec (50 sec for a stroke). This operation corresponds to a 0.1 sec timing resolution with 5 μm track connection accuracy. More details and the flight data are described in Ref. [27].

The calorimeter consisted of a stack of 32 OPERA films, 10 lead plates (0.5 mm thickness), and 17 lead plates (1.0 mm thickness). The total thickness and radiation length were 31.9 mm and 4.0 X_o, respectively.

3.   Balloon experiment in 2011

For this first experiment, the following equipment was installed on a gondola: emulsion chamber, star camera, temperature meters, pressure meter, GPS systems, and a battery, as shown in Fig. 2. The emulsion chamber was installed in a 1 mm thick aluminum enclosure removed around the upper part of the chamber for light shielding and waterproofing without a pressure vessel, to reduce thickness (g/cm^2) and total weight.

The balloon launch was performed on 8 June 2011 from the Taiki Aerospace Research Field (TARF) [24]. The geomagnetic rigidity (around 8 GV for 50% cutoff) was calculated by the GAPS Collaboration at the balloon altitude [25]. Figures 3 and 4 show the flight path, the altitude, and the residual atmospheric pressure. The balloon was launched at 05:04 Japan Standard Time (JST). Level flight at 34.7 km altitude and 6.5 hPa residual atmospheric pressure (6.6 g/cm^2 atmospheric depth) started from 7:14. System shutdown was initiated at 8:40 and the gondola was released at 08:50. The gondola splashed down at sea at 09:24 and was successfully recovered at 9:43. The total flight duration for this experiment was 4.3 hours, with 1.6 hours at an altitude of 34.7 km.

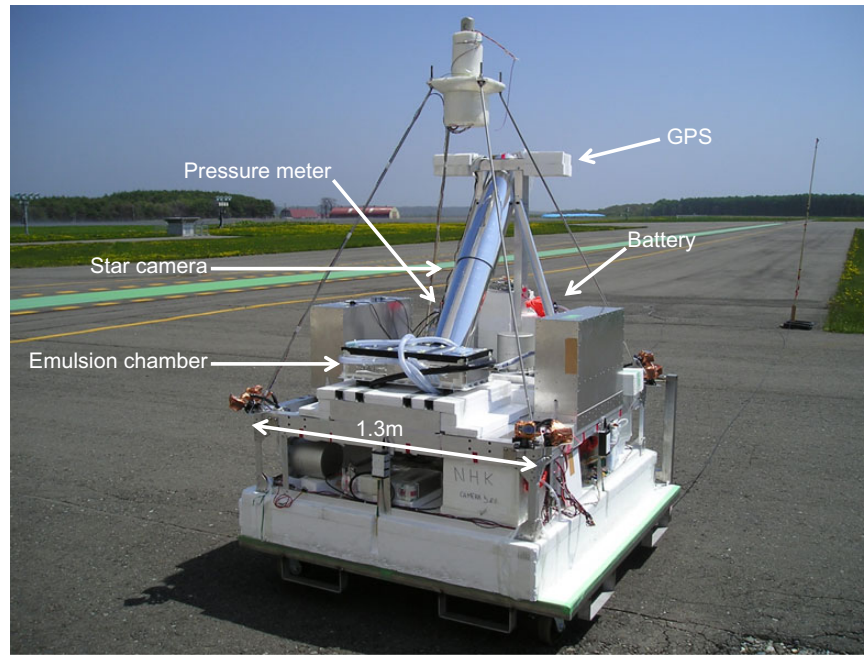[1] NITTO DENKO, Printac F.
[2] TERAOKA SEISAKUSHO, 7692 #12.

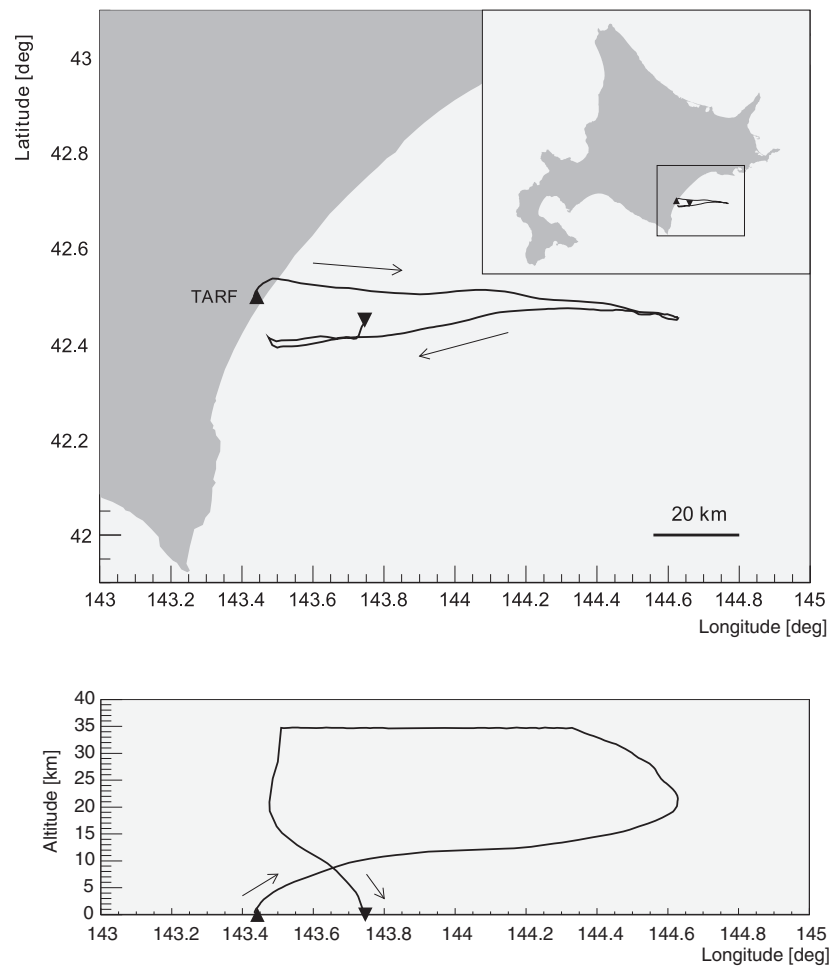**Fig. 2.** The balloon gondola (before insulating).

Fig. 3. Flight path in longitude (horizontal axis) and latitude (vertical axis). Bottom figure shows the flight path in longitude (horizontal axis) and altitude (vertical axis).
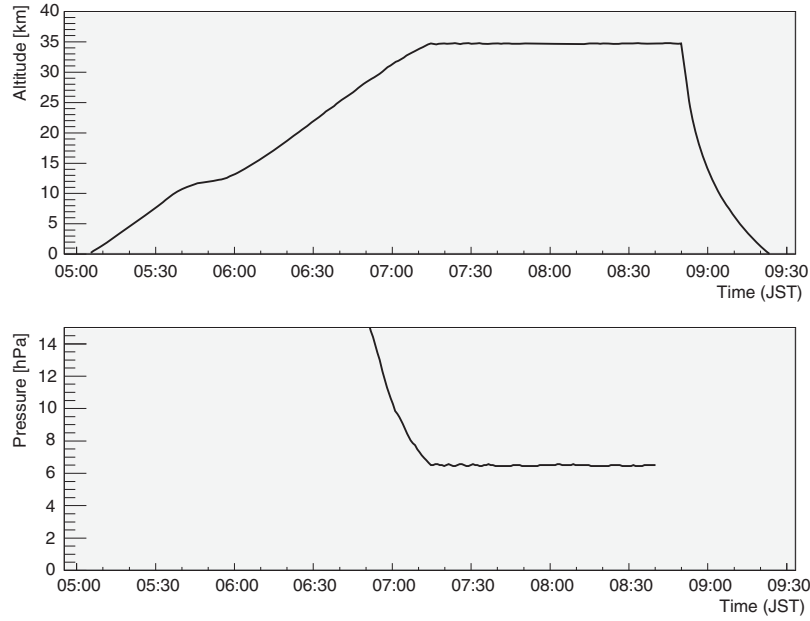
Fig. 4. The altitude and the residual atmospheric pressure as a function of time.

4. Data analysis

4.1. *Emulsion track readout and reconstruction*

Readout of all the emulsion track data was performed by means of an automated emulsion scanning system, SUTS [15,16]. Figure 5 shows the position distribution of the readout tracks. After several tests close to each edge of the film, the fiducial scanning area was set to be 0.0, 0.5, 1.0, and 1.5 mm from the left, top, right, and bottom edges of the film (the red square in Fig. 5 shows the edge of the film and the gray area shows the scanning area). Stable scanning was performed within the fiducial area. The angular acceptance for track recognition was set at $|\tan\theta_{\mathrm{proj}}| < 1.0$ ($|\theta_{\mathrm{proj}}| < 45°$), where θ_{proj} is the projection angle for a normal vector at the surface of the emulsion film. The conventional angular acceptance with the scanning system is $|\tan\theta_{\mathrm{proj}}| < 0.6$ ($|\theta_{\mathrm{proj}}| < 31°$). The angular acceptance, $|\tan\theta_{\mathrm{proj}}| < 1.0$, across the whole area of the emulsion film is the first trial for gamma-rays with large incident angle. The total number of readout tracks per emulsion layer was $\sim 10^9$ tracks. Out of these tracks, $10^2 - 10^3$ beginning tracks of electron pairs were expected.

The track reconstruction was performed based on track pattern matching with positions and angles. This offline track reconstruction procedure is referred to as "connecting" tracks. The details of track reconstruction are described elsewhere [28–30].

The readout tracks were clustered for each scanned layer. The clustered tracks were connected between both sides of the base of each film (base track). The base tracks were connected between films. The determination of the connection allowance (the agreement of position and angle) between films took account of the angle dependence and multiple Coulomb scattering for low-momentum tracks. With the allowance, tracks were connected up to $|\tan\theta_{\mathrm{proj}}| = 1.0$ and down to $25\,\mathrm{MeV}/c$. To recover the track-finding inefficiency in a single film, track connection between films was performed every three films at maximum. Tracks connected between films were folded in across all connected films. For films #1 to #16, a total of 7.9×10^7 tracks were folded in. Figure 6 shows the number of tracks from films #1 to #16 for each processing step.
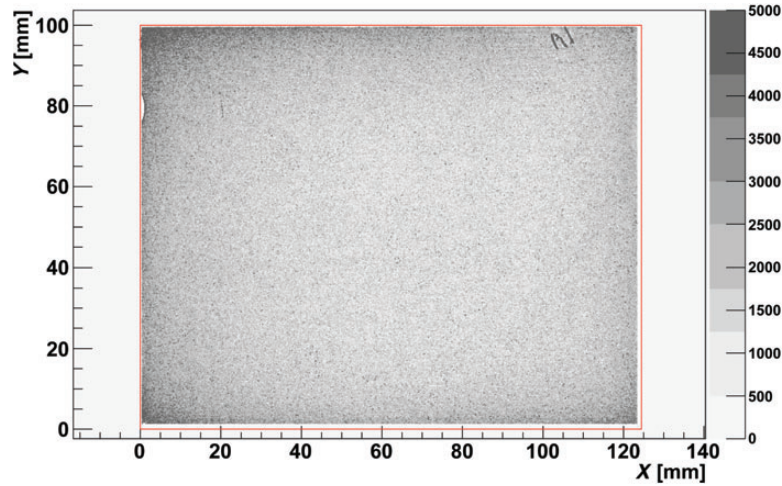
Fig. 5. Position distribution of readout tracks. The red square shows the size of the emulsion film. The gray level scale shows the number of readout tracks per field of view ($230 \times 228 \, \mu m^2$). The total number of readout tracks in this layer was 8.0×10^8 (film #67, upstream side).
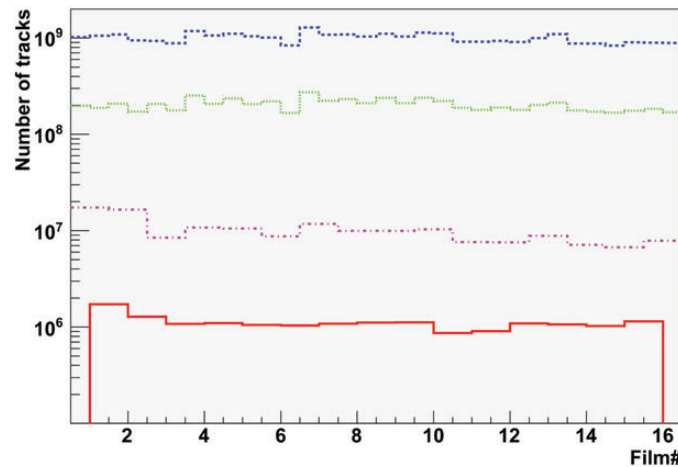

Fig. 6. Number of tracks from films #1 to #16 for each processing step. Dashed line (blue) shows the number of readout tracks. Dotted line (green) shows the number of clustered tracks. Dot-dashed line (pink) shows the number of connected tracks between both sides of the film base. Solid line (red) shows the number of connected tracks between adjacent films.

4.2. Track connection accuracy

A schematic illustration of the track position and angle connection between films is shown in Fig. 7. Figure 8 shows the distributions of the position difference (shown as "dx" in Fig. 7) for each projection, fitted with a Gaussian function with "σ"s of 0.75 μm and 0.76 μm for the two projections. Figure 9 shows the distributions of the obtained "σ"s for the connected films. The variations in the distributions were mainly due to the difference of extrapolated distance with different geometry between #1–#10 and #11–#16 (see Sect. 2 and Fig. 1). Basically, the fine position accuracy was obtained across all connected films. Figure 10 shows the distributions of angle difference (shown as "$d\theta_x (\sim d(\tan \theta_x))$" in Fig. 7) for each projection. The values of σ obtained by fitting with a Gaussian function were 4.2 mrad (0.24°) and 4.6 mrad (0.26°) for each projection. Figure 11 shows
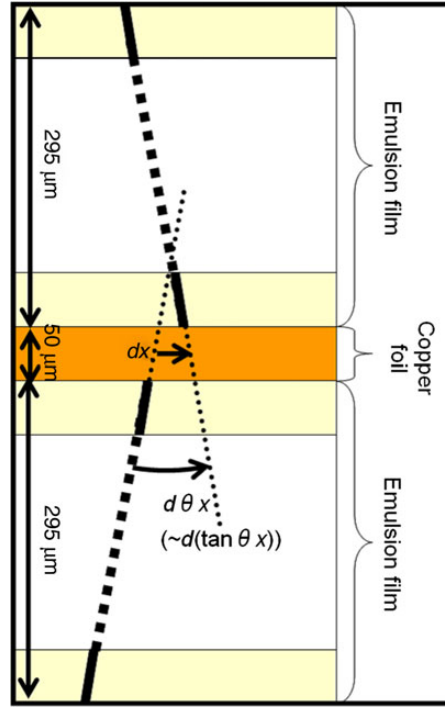
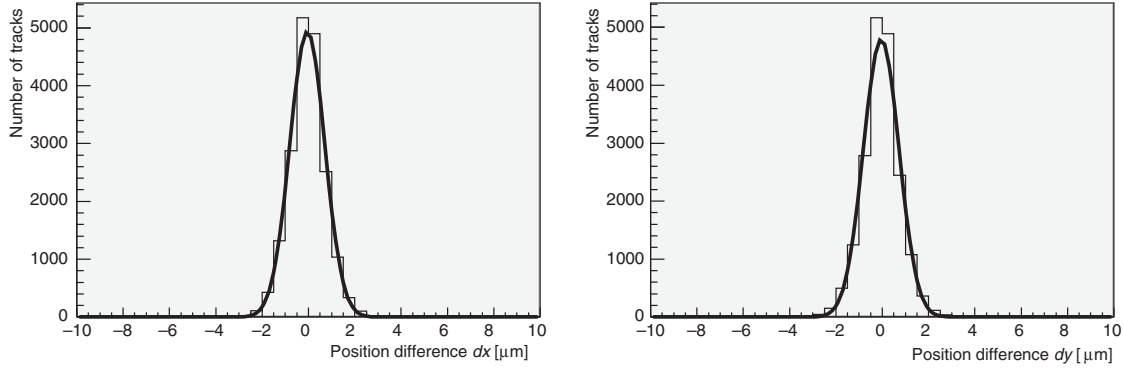**Fig. 7.** Schematic view of track connection between films.

Fig. 8. Distributions of position differences for each projection (left: X-projection, right: Y-projection) fitted with a Gaussian function with σ of 0.75 µm in X-projection and 0.76 µm in Y-projection, respectively (films #12–#13, $\tan\theta < 0.1$).

the distributions of the obtained "σ"s for the connected films, indicating good angular accuracy for all connected films. The variations were mainly due to the difference in scanning systems.

Figure 12 shows the angular difference σ as a function of incident zenith angle θ in the transverse and longitudinal directions for each track. Here, the angular error ($\sigma_{\tan\theta_{\text{proj}}}$) is expressed by the propagating horizontal position error (σ_x) and vertical position error (σ_z). By propagating the angular error to the angular difference error ($\sigma_{d(\tan\theta_{\text{proj}})}$), the angular difference error is expressed as follows:

$$\sigma_{d(\tan\theta_{\text{proj}})} = \frac{2}{dz}\sqrt{\left(\sigma_x\right)^2 + \left(\sigma_z \cdot \tan\theta_{\text{proj}}\right)^2},\tag{1}$$

where dz corresponds to the thickness of the emulsion film base. Only the second term under the square root is dependent on projection angle. The transverse direction, which is the direction with
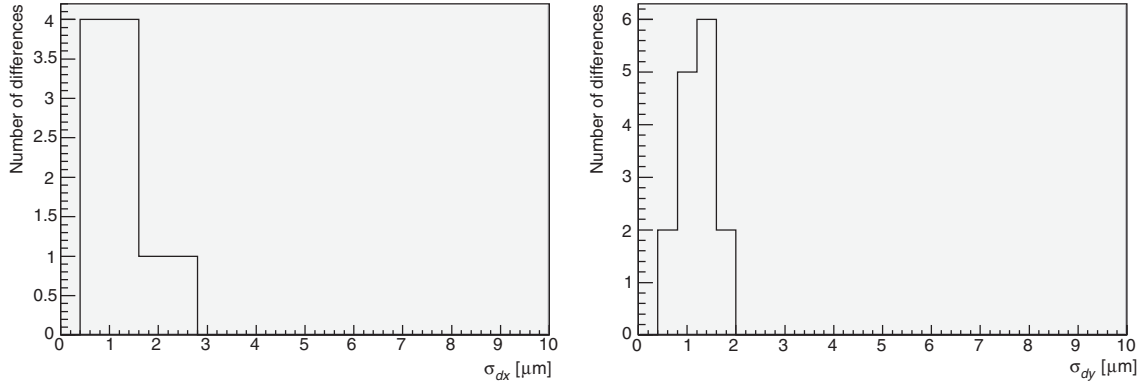
Fig. 9. Distributions of position difference "σ"s for connected films #1–#2 to #15–#16, $\tan\theta < 0.1$ (left: X-projection, right: Y-projection).
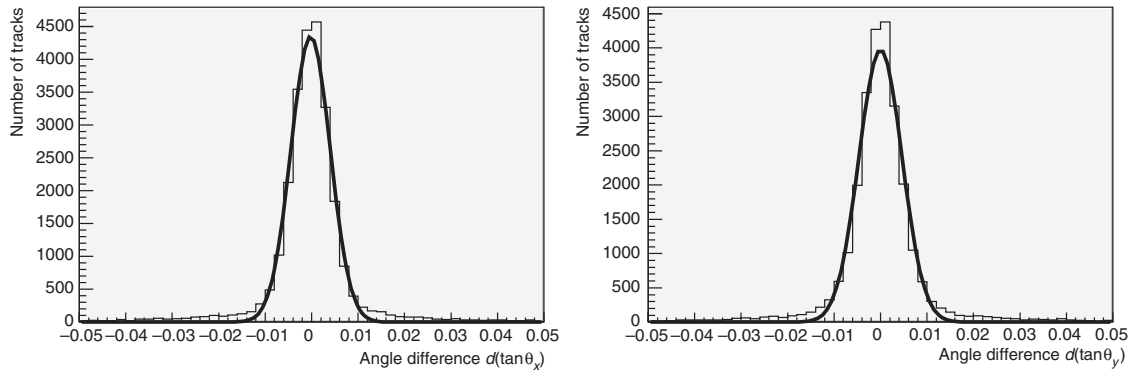

Fig. 10. Distributions of angular differences for each projection (left: X-projection, right: Y-projection) fitted with a Gaussian function, resulting in σ of 4.2 mrad in X-projection and 4.6 mrad in Y-projection, respectively (films #12–#13, $\tan\theta < 0.1$).
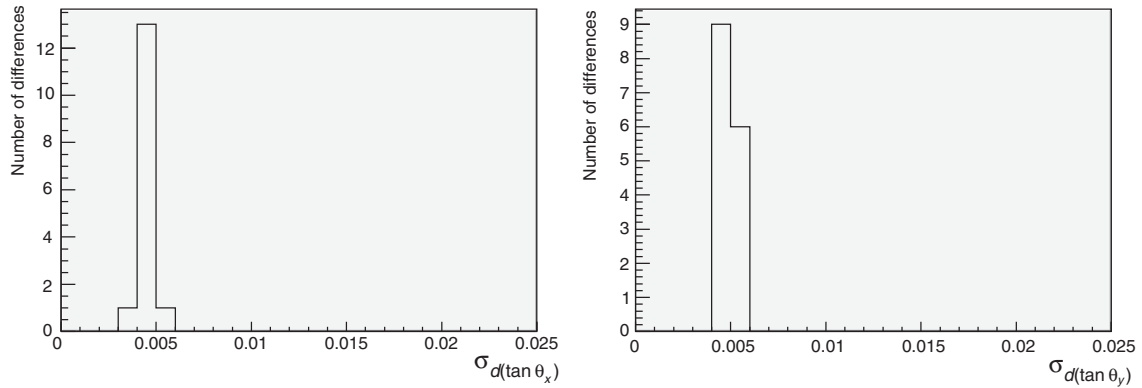

Fig. 11. Distributions of angle difference "σ"s for connected films #1–#2 to #15–#16, $\tan\theta < 0.1$ (left: X-projection, right: Y-projection).

$\tan\theta_{\mathrm{proj}} = 0$, is quite constant for the incident zenith angle. The angular error was obtained as 3.0×10^{-3} (approximately 3.0 mrad). The longitudinal direction, which is the direction with a projection angle equal to the incident zenith angle, exhibits incident zenith angular dependence. A fitted curve using Eq. (1) with horizontal position error (σ_x) and vertical position error (σ_x) as parameters
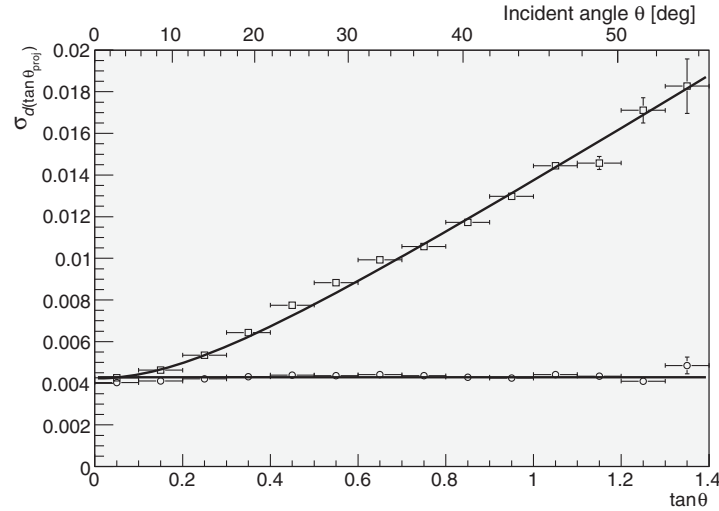
Fig. 12. Angle difference σ as a function of incident zenith angle θ for transverse ($\circ$) and longitudinal ($\square$) directions for each track. The solid line shows the fitting curve with Eq. (1) (films #12–#13).

fits the data well, as shown in Fig. 12. The obtained fitting parameters were $0.42\,\mu$m for the horizontal position error and $1.37\,\mu$m for the vertical position error.

The angular difference error was dominated by the vertical position error at large incident zenith angles. The curved field of view of the SUTS microscope was a possible cause of the vertical position error. The vertical position difference in the focal plane between the center and the edge of the microscope was $3\,\mu$m (peak to peak). This was equivalent to the observed vertical position error. The field curvature effect can be corrected since the vertical position difference in the focal plane is determined by the horizontal position of the recognized track. By correcting for the field curvature effect, the vertical position error could be reduced, resulting in an improved incident zenith angle dependence.

4.3. Track-finding efficiency in a single film

The track-finding efficiency in a single film was evaluated by connecting tracks above and below a middle film and checking for the existence of connectable tracks in the middle film (Fig. 13). Figure 14 shows the position distributions of the track efficiency for each projection. Uniform efficiency was obtained across the whole area of the emulsion film. Figure 15 shows the distribution of track efficiency across all connected films. Uniform efficiency was obtained across all the connected films. Figure 16 shows the efficiency as a function of the incident zenith angle θ. A track efficiency of 78% was obtained at $\tan\theta < 0.1$ and 64% at $1.0 < \tan\theta < 1.1$. The main component of the inefficiency at large zenith angles was the reconstruction inefficiency at the base track. By taking account of the angular dependence for an acceptable angular difference of $0.12\tan\theta + 0.05$ rad instead of 0.05 rad ($2.87°$) constant value at the base track reconstruction, a track efficiency of 95% at $1.0 < \tan\theta < 1.1$ was obtained. Although it is important to improve the angular dependence, high efficiency was achieved at large zenith angles. By installing a high-sensitivity emulsion gel film in part of the emulsion chamber for this experiment, higher efficiency and higher uniformity for the incident zenith angle was achieved.
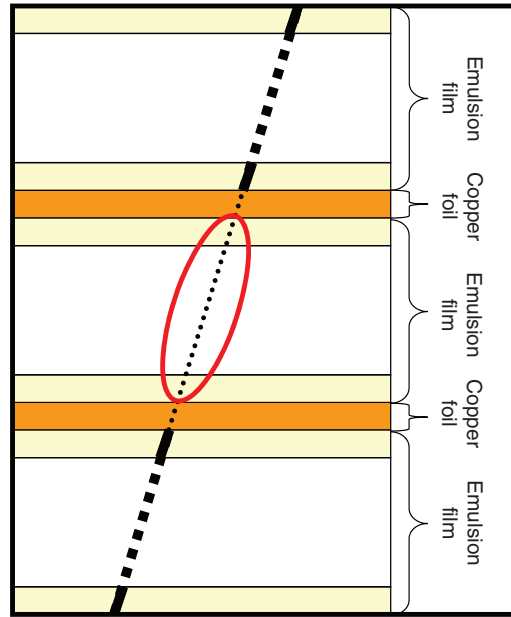
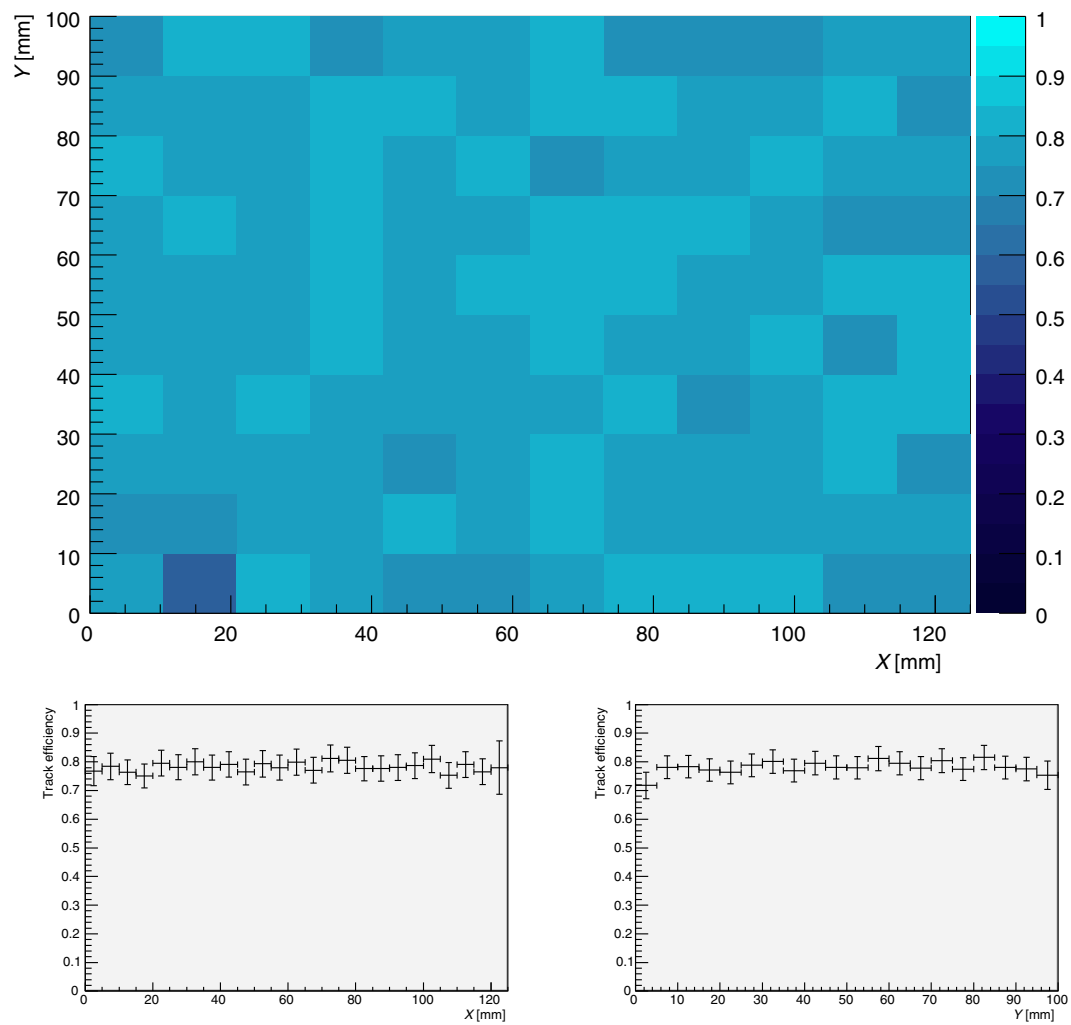**Fig. 13.** Schematic view of the evaluation of track-finding efficiency.

Fig. 14. Track-finding efficiency as a function of position (top: X–Y space, left bottom: X-projection, right bottom: Y-projection, film #5, $\tan\theta < 0.1$).
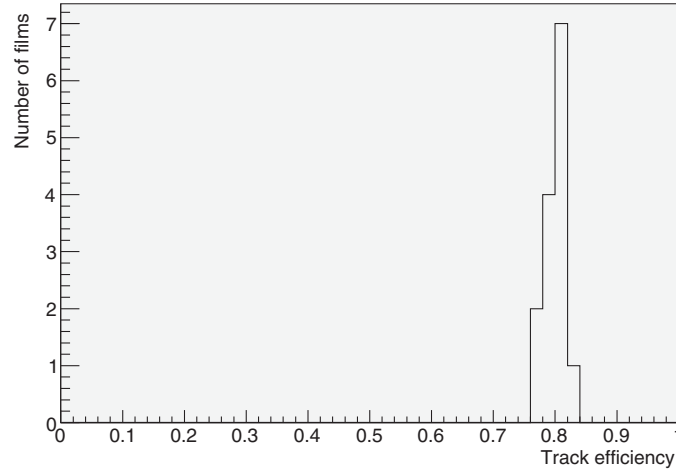
Fig. 15. Distribution of track efficiency for each connected film #2 to #15, $\tan\theta < 0.1$.
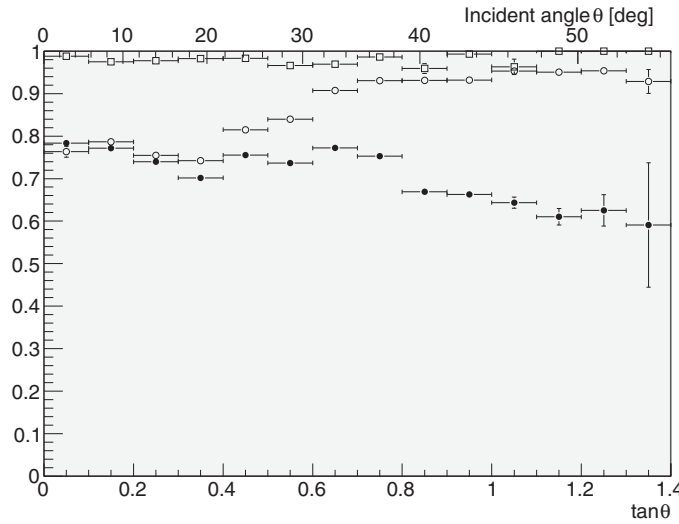
Fig. 16. Track-finding efficiency as a function of incident zenith angle θ. Filled circles (●) show the track efficiency (film #5). Open circles (○) show the track efficiency that was achieved by gradually relaxing the acceptable angular difference for incident zenith angles in base track reconstruction (film #5). Open boxes (□) shows high-sensitivity emulsion gel film installed in part of the emulsion chamber (shifter 3rd stage, film #3, $5 \times 5\,\mathrm{mm}^2$).

4.4.   Detection of γ-ray events

The identification and selection of γ-ray events was based on the electron pair topology requirement, as displayed in Fig. 17 for a $5 \times 5\,\mathrm{mm}^2$ region in 10 films extracted from the data volume.

Out of 7.9×10^7 reconstructed tracks, 2.3×10^5 tracks were selected as downward starting from a film in the middle of the converter (selection criteria: starting at film #7 downward, anticoincidence with above 3 films (films #8, 9, 10), having at least five track segments). Out of these 2.3×10^5 tracks, 1.1×10^3 events were selected as follows: the tracks having a nearby partner track that was downward starting (selection criteria: starting at film #7 or below, having at least five independent track segments) with a near position ($<75\,\mu\mathrm{m}$) and a similar angle ($<75\,\mathrm{mrad}$) at the start of the track segment. Out of the 1.1×10^3 events, 153 events were selected as γ-ray events by doing a display check. The display check was done for each event using a 3D viewer for reconstructed tracks
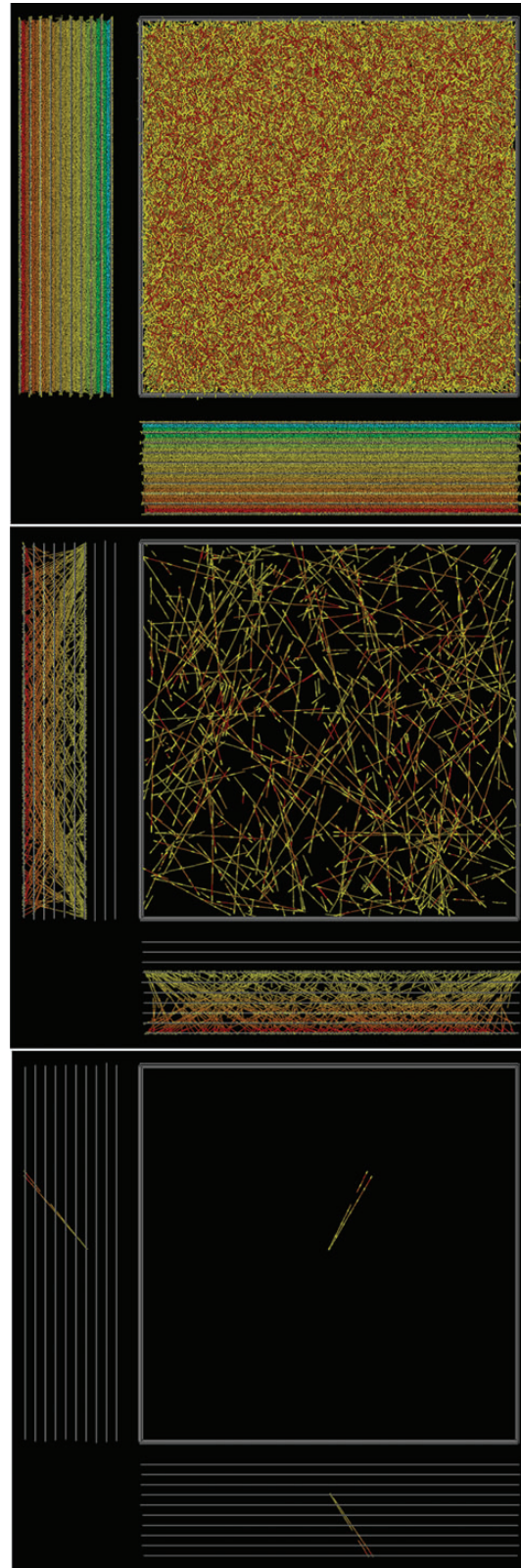
Fig. 17. Example of the detection procedure for a γ-ray event. Tracks in a $5 \times 5\,\text{mm}^2$ region of 10 films (from #1 to #10, 4.5 mm) are shown for each projection. White squares and lines show the area and location of each film. Track segments are shown with different colors for each film. The top figure shows 2.2×10^4 reconstructed tracks in this volume. The middle figure shows 242 downward-starting tracks from film #7. The bottom figure shows the selected event.

Table 1. Summary of the γ-ray event detection procedure.

Procedure	Number of selected tracks or events
Reconstructed tracks	7.9×10^7
Downward-starting tracks	2.3×10^5
Tracks with a nearby partner	1.1×10^3
Display check	153
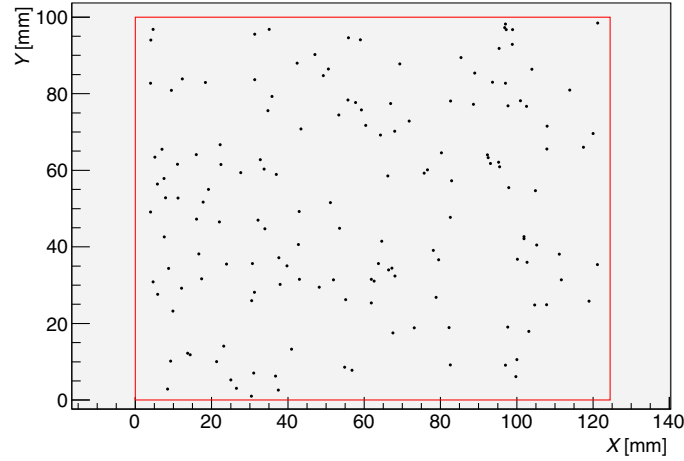
Fig. 18. Position distribution of detected γ-ray events. The red square shows the size of the emulsion film.
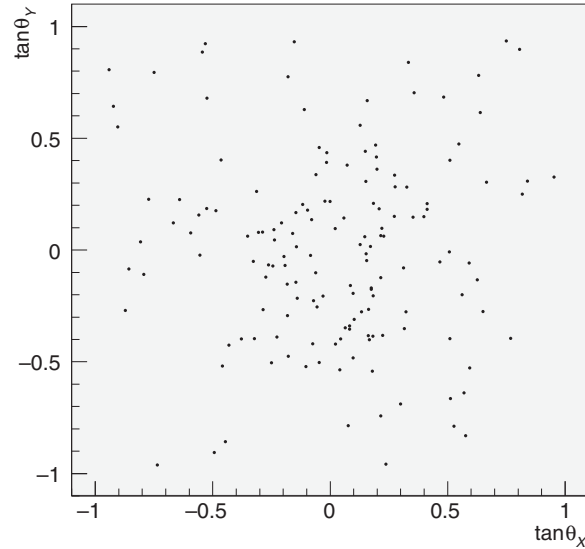
Fig. 19. Angular distribution of detected γ-ray events.

and events (Fig. 17 shows snapshots of the 3D viewer). The main reason for events to be rejected by the display check was misreconstruction due to a near-miss of the penetrating track to a downward-starting track, which could be clearly distinguished.

Table 1 summarizes the event detection procedure. Figures 18 and 19 show the position and angular distributions of the detected γ-ray events. We performed a systematic detection of γ-ray events across the whole emulsion area and up to 45° for each projection angle in absolute values ($|\tan\theta_{\mathrm{proj}}| < 1.0$). By applying this procedure for each film, γ-ray event detection can be performed for all converter
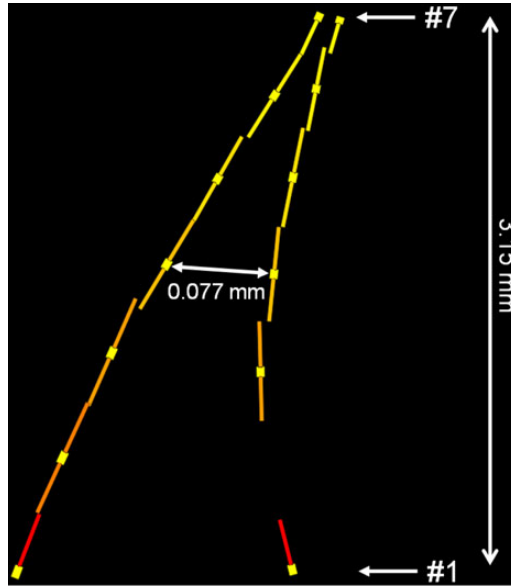
Fig. 20. An example of γ-ray event energy reconstruction. The incident zenith angle of this event was $9.748°$. A left side track was measured as 60^{+20}_{-12} MeV/c corresponding to 25% relative error in inverse momentum. A right side track was also measured as 32^{+9}_{-6} MeV/c corresponding to 22% relative error in inverse momentum. From these momenta, the γ-ray energy was reconstructed to be 92^{+22}_{-13} MeV corresponding to $+24\%$ and -14% relative errors.

films. The selection task could be accelerated by automating rejection of misreconstructed events. Moreover, by using emulsion films with higher track efficiency and higher signal-to-noise ratio, like the high-sensitivity emulsion gel films installed in part of the chamber for this experiment, the selection effort can be substantially reduced in subsequent experiments.

4.5.   *Reconstruction of γ-ray energy*

A systematic energy reconstruction was tried for all detected γ-ray events. By measuring the momenta of an electron pair with multiple Coulomb scattering, the γ-ray energy can be reconstructed. The first momentum measurement and systematic momentum measurement with NETSCAN have been described elsewhere [28,29,31]. The angular method was applied to measure the momentum with multiple Coulomb scattering. The angular method measures the deviation of the scattering angle. To minimize measurement error of the scattering angle (corresponding to maximizing the detectable momentum), the angle measurement was divided into transverse and longitudinal directions. The measurement error in the scattering angle was evaluated from the number of penetrating tracks as a function of incident zenith angle for each projection. The accuracy of the momentum measurement depends on the number of measured scattering angles, the momentum, and the incident zenith angle. By adding measurement films, the measurement accuracy of the momentum could be improved.

Figure 20 displays an example of energy reconstruction for a γ-ray event. The left track was measured at 60 MeV/c with a 25% relative error in inverse momentum. The right track was measured at 32 MeV/c with a 22% relative error in inverse momentum. From these momenta, the γ-ray energy was reconstructed to be 92 MeV with a relative error of $+24\%$ and -14%. In this analysis, for 306 tracks of the selected 153 events, a systematic momentum measurement was attempted. Out of these 306 tracks, 263 tracks were measured, 86% of the total. For the remaining 43 tracks (14%), a lower

Table 2. Summary of track momentum measurements.

Number of tracks	306	
Measured	263	86%
Lower limit	43	14%

Table 3. Summary of γ-ray energy reconstruction.

Number of events	153	
Reconstructed	112	73%
Lower limit	41	27%
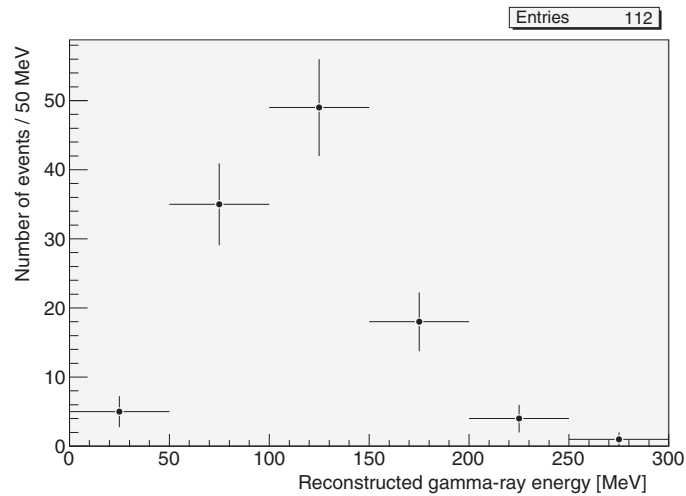
Fig. 21. Reconstructed γ-ray energy spectrum.

limit of momentum was set due to insignificant scattering. In the event base, out of 153 events, 112 events, 73%, had reconstructions of γ-ray energies. For the other 41 events (27%) a lower limit of γ-ray energy was assigned. Tables 2 and 3 summarize the momentum measurement and energy reconstruction. By using the calorimeter located at the bottom part of the emulsion chamber, the measurement accuracy could be improved and events with a lower limit could be recovered. Figure 21 shows the reconstructed γ-ray energy spectrum. Systematic momentum measurement and energy reconstruction were performed with the balloon chamber. In this analysis, the detection of γ-ray events was performed down to the 50 MeV region.

4.6.   Event detection efficiency and kinematics comparison with Monte Carlo simulation

Monte Carlo (MC) simulation was used to evaluate the detection efficiency of γ-ray events and for a comparison with electron pair kinematics.

Electron pairs in the emulsion chamber were generated by a Geant4.9.5 [32] simulation using the G4BetheHeitlerModel conversion model. MC events were deconstructed to the scanned track segment level. The readout position error, readout angle error, and readout efficiency were included based on the scanned data used in this analysis. Deconstructed events with readout response were reconstructed by the same procedure as for the scanned data in this analysis.
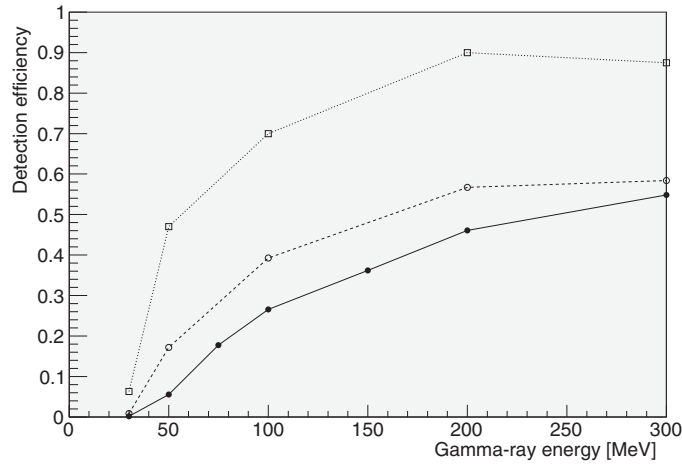
Fig. 22. Detection efficiency of events as a function of γ-ray energy for each criterion (at normal incidence with 7 films). The solid line shows the detection efficiency in this analysis. The dashed line represents additional searching for events with a wider opening angle. The dotted line corresponds to emulsion films with higher track efficiency (100%), like the high-sensitivity emulsion gel films installed in part of the chamber in this flight.

The survival efficiency was evaluated as the detection efficiency. Figure 22 shows the detection efficiency as a function of γ-ray energy for each criterion. By using higher-sensitivity emulsion films, like the high-sensitivity emulsion gel films installed in part of the chamber for this experiment, a detection efficiency up to 70% at 100 MeV and up to 90% at 200 MeV could be achieved in a subsequent flight. Moreover, the γ-ray energy threshold could be lowered since the detection criteria could be relaxed by using emulsion films with higher track efficiency.

The kinematics of electron pairs for the energy-reconstructed γ-ray events were compared with MC events. For this comparison, MC events were distributed according to the reconstructed γ-ray energy spectrum and normalized to the number of energy-reconstructed γ-ray events. The MC truth was used. The bias of the detected γ-ray events was included, whereas the bias of the energy-reconstructed γ-ray events was not included. In this comparison we included momentum, opening angle, energy ratio, and invariant mass, as shown in Fig. 23. The opening angle is in units of $\omega_0 = mc^2 E_\gamma / E_{e^+} E_{e^-}$, where mc^2 is the electron rest mass, E_γ is γ-ray energy, and E_{e^+} and E_{e^-} are the energies of a positron and an electron. The energy ratio is defined as $E_1/(E_1 + E_2)$, where E_1 and E_2 are the energy of a positron and an electron and $E_1 < E_2$. Slight differences are observed between the data and the MC primarily due to the detector response and the bias in the reconstructed energies in MC γ-ray events. Basically, the data trend was reproduced by the MC.

4.7. Timestamp

By connecting γ-ray event tracks to the multi-stage shifter, a precise arrival time (timestamp) could be assigned to each event. The 153 γ-ray events detected were followed down to film #1 or #2 of the interface to the timestamper. Out of 153 detected events, 145 were followed down to the interface films for both tracks in an event. The other eight events were followed down to the interface films for one side track in an event. Table 4 summarizes the follow-down results. All the detected γ-ray events were performed to follow down to interface films. Attempts were made to connect all the followed-down event tracks to the first stage of the multi-stage shifter. Ninety-eight events were timestamped for both tracks in an event with a consistent timestamp for both tracks ($\odot$). Thirty events
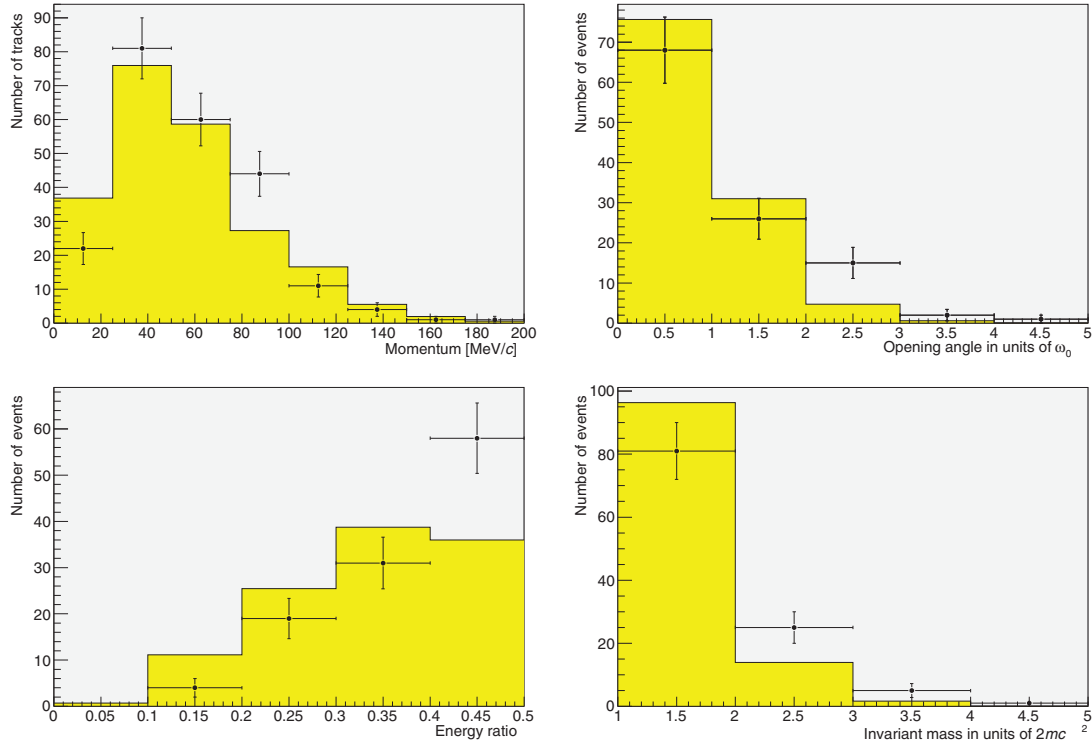
Fig. 23. Data MC comparison of kinematic variables of electron pairs. The dots with error bars show the data. The solid line histograms show the MC. (Top left) Momentum distribution of positrons and electrons. (Top right) Distribution of opening angle in units of ω_0. (Bottom left) Distribution of energy ratio $E_1/(E_1 + E_2)$. (Bottom right) Distribution of invariant mass in units of $2mc^2$.

Table 4. The follow-down results.

Detected	153		
Followed down	153	Both tracks	145
		One side track	8

were timestamped for one side track in an event ($\circ$). Fifteen events were timestamped for both tracks but had an inconsistent timestamp between the two tracks ($\triangle$). Ten events were not timestamped ($\times$). Table 5 summarizes the timestamping results.

Fifteen events ($\triangle$) had inconsistent timestamps between both tracks in an event. By doing a check by eye with a microscope, the readout inefficiency and reconstruction inefficiency could be recovered. For 15 events ($\triangle$), an eye check was done around the conversion point (films #6, 7, 8, 9, 10) to confirm the validity of the γ-ray event. Out of these 15 events, 12 events were confirmed as γ-ray events due to downward starting and splitting into two tracks. These 12 confirmed events were classified as mis-timestamped events. The remaining three events were judged to be fakes due to at least one track penetrating upstream of the conversion point. By using emulsion films with higher track efficiency, these fake γ-ray events could be rejected as part of the detection procedure.

For 113 double track events ($\odot$, $\triangle$), the contamination ratio of fake γ-ray events was obtained as 2.7% $\left(\frac{3}{113}\right)$. The event mis-timestamping ratio was calculated to be 10.9% $\left(\frac{12}{113-3}\right)$. The track mis-timestamping ratio was 5.6% $\left(1 - \sqrt{1 - \frac{12}{113-3}}\right)$. Out of 30 events ($\circ$), 0.8 events (2.7%) were

Table 5. Timestamp event statistics.

Timestamp classification		Events	Eye check	
Both tracks, consistent	⊙	98		
One side track	○	30		
Both tracks, inconsistent	△	15	Confirmed	12
			Fake	3
Not timestamped	×	10		

Table 6. Event detection reliability, timestamp reliability, and timestamp efficiency.

	⊙, ○, △, ×	⊙, ○
Event detection reliability	97%	99%
Timestamp reliability	95%	99%
Timestamp efficiency	93%	85%

expected to be fake γ-ray events and 1.6 events (5.6%) were expected to be mis-timestamped events. Out of 10 events ($\times$), 0.3 events (2.7%) were expected to be fake γ-ray event.

For all 153 events ($\odot$, $\circ$, $\triangle$, $\times$) the estimated reliability of a γ-ray event was 97% $\left(1 - \frac{3+0.8+0.3}{153}\right)$. The timestamp reliability was estimated to be 95% $\left(1 - \frac{\frac{12}{2}+1.6}{143-3.8}\right)$, with a timestamp efficiency of 93% $\left(\frac{143-3.8}{153-4.1}\right)$. By selecting the timestamp classification, even though the timestamp efficiency is reduced slightly, the reliability of γ-ray event detection and the timestamp reliability could be improved. For 128 events ($\odot$, $\circ$), the reliability of γ-ray event detection was found to be 99% $\left(1 - \frac{0.8}{128}\right)$. The timestamp reliability was estimated to be 99% $\left(1 - \frac{1.6}{128-0.8}\right)$ and a timestamp efficiency of 85% $\left(\frac{128-0.8}{153-4.1}\right)$ was achieved. Table 6 summarizes the reliability of γ-ray event detection, the timestamp reliability, and the timestamp efficiency. By using emulsion films with higher track efficiency for the multi-stage shifter, the timestamp efficiency could be improved.

The 3rd stage of the multi-stage shifter moved continuously during the balloon flight from an altitude of 22 km till system shutdown. By connecting the tracks to the 3rd stage of the shifter, timestamps were obtained to within sub-second accuracy. Out of 128 events ($\odot$, $\circ$) with the 1st stage timestamp, 41 events had timestamps from 22 km altitude to system shutdown. Out of these 41 events, 30 events were connected to the 3rd stage. Timestamping of γ-ray events down to the 3rd stage was performed with 98% timestamp reliability and with 62% timestamp efficiency.

The timestamp inefficiency was mainly due to edge effects and track-finding inefficiency of the film. By enlarging the timestamper area to overlap the converter area and by using emulsion films with higher track efficiency and higher signal-to-noise ratio, like the high-sensitivity emulsion gel films installed in part of the chamber in this experiment, the timestamp efficiency could be improved.

4.8.   Discrimination of γ-rays produced in the converter

The detected γ-ray events include events produced in the converter by hadrons or electrons. Hadron- and electron-induced events were searched for from the 30 γ-ray events with a 3rd stage timestamp.

Hadron-induced events were required to have a timing coincidence and a convergence with other tracks for each γ-ray event. By setting a ± 1 sec time window, an average of 110 tracks were selected for each γ-ray event. For the selected tracks, requiring a convergence with at least two tracks in
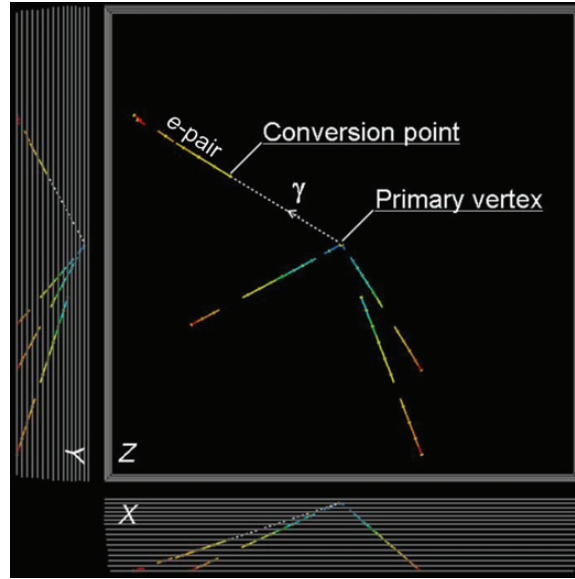
Fig. 24. A hadron-induced event for each projection with $1.2 \times 1.2\,\mathrm{cm}^2$ in 16 films (0.6 cm). The multiplicity of this event was 3 tracks.

the converter, six events were discriminated as hadron-induced events. One of the discriminated hadron-induced events is shown in Fig. 24. The multiplicities of the discriminated events were three (one event), five (two events) and ≥ 10 (three events). Since the discriminated events had higher multiplicity, clear event detection was performed. For the lowest multiplicity event (i.e., three), an eye check with a microscope was made around the primary vertex. Additional minimum ionizing tracks and a nuclear fragment were found over the scanning angle acceptance. Thus, this event was clearly confirmed as being a hadron-induced event.

Electron-induced events were searched for by requiring a coincidence with timing, position, and angle for each γ-ray event. A γ-ray is typically emitted in a narrow angle from the bremsstrahlung of an electron. Thus electron-induced events are expected to exhibit a small position difference and small angle difference between the electron and the γ-ray event. Figure 25 shows the distribution of position difference and angle difference for tracks selected within a ± 1 sec time window for each γ-ray event. Electron-induced events were clustered around the region of small position difference and small angle difference, and were clearly separated from random coincidences. In this case, by setting a <1 mm position difference and <0.05 rad angle difference, five electron-induced events were clearly discriminated without inefficiency and chance coincidences. One of the discriminated electron-induced events is shown in Fig. 26. An offline triggering method was created using the data from reconstructed events and tracks and discrimination of γ-rays produced in the converter was achieved.

The identification of γ-rays produced in the converter not only suppressed the background, but could also be useful for calibrating direction, timing, energy, polarization, and detection efficiency. The angular resolution of γ-ray events was evaluated (Fig. 27) with the hadron-induced events by using convergence[3] and with electron-induced events by using parallelism[3]. A high angular resolution was achieved with the flight data. The timing resolution of the γ-ray events was evaluated

---

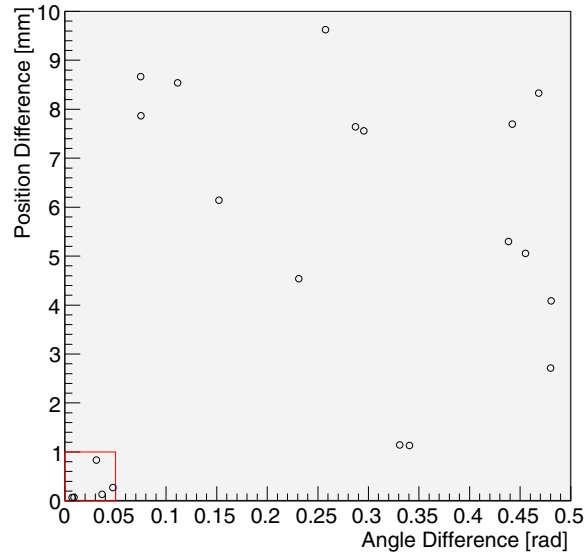[3] The discrimination criteria are not tight for γ-ray angular resolution.

Fig. 25. Distribution of angular difference and position difference for tracks selected with ±1 sec time window for each γ-ray event. The red box shows the signal region.
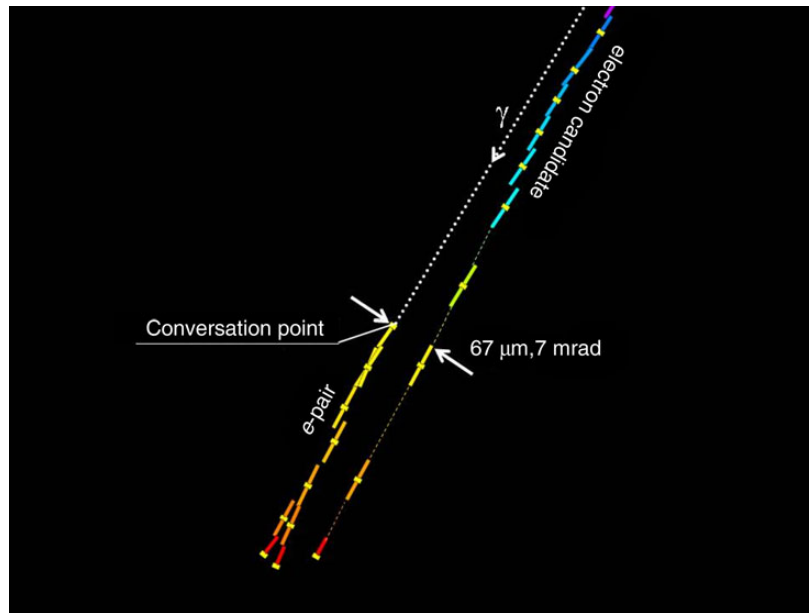

Fig. 26. An example of an electron-induced event.

(Fig. 28) with the hadron-induced events by comparing the γ-ray timing with the timing center of the hadron tracks[4] and with the electron-induced events by comparing the γ-ray timing with the timing of the electron candidate[4]. A 0.2 sec timing resolution was obtained. A timing resolution of <1 sec was required to determine the γ-ray arrival direction and hence a sufficient timing resolution was achieved with the flight data. A method to check and calibrate the γ-ray data using the flight data was created.

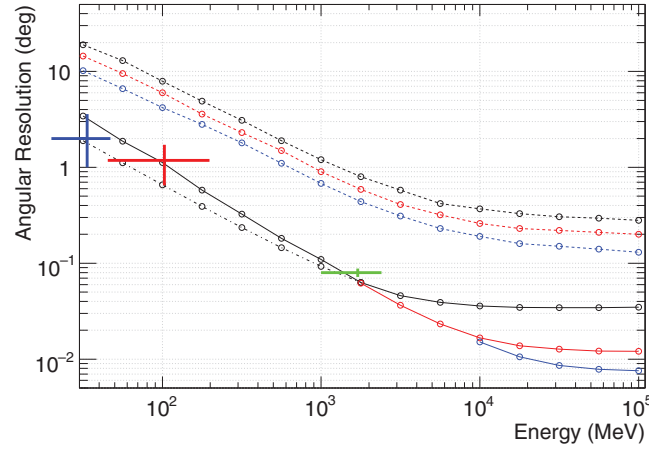[4] The discrimination criteria are not tight for γ-ray timing resolution.

Fig. 27. Angular resolution as a function of γ-ray energy. Dashed lines (black: total, red: front, blue: back) show the angular resolution of Fermi-LAT [33]. Solid lines show MC simulation of the emulsion γ-ray telescope (black: 1 film, red: 2 films, blue: 3 films). Dot-dashed line shows MC simulation of the emulsion γ-ray telescope with grain-by-grain measurement around the conversion point. Data points with error bars are γ-ray telescope experimental data (red: this work, green: LEPS/SPring-8, blue: UVSOR). This work shows results for the 0–47° incident zenith angle range. The others were at normal incidence.
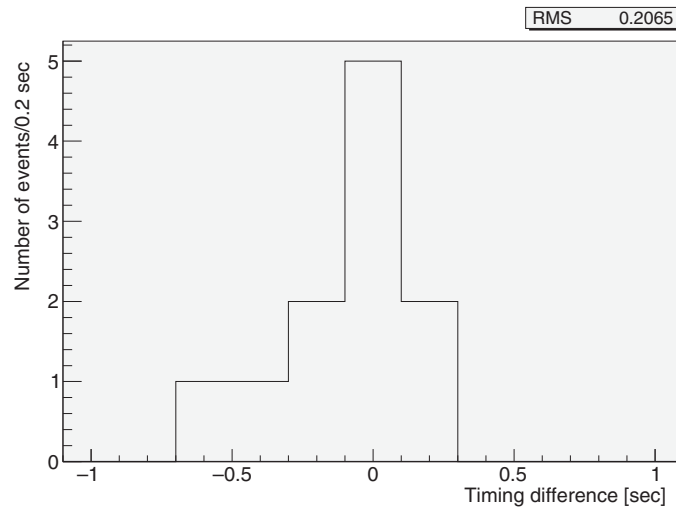

Fig. 28. Timing resolution of γ-rays for 45–245 MeV energy range and for 0–47° incident zenith angle range.

4.9. Atmospheric γ-ray measurements

Figure 29 shows the time profile of γ-ray events, excluding the events produced in the converter. The residual atmospheric pressure below 13 hPa was measured by a pressure meter, which was absolutely calibrated to within 1% accuracy. Above 13 hPa, the GPS altitude data were converted to atmospheric pressure by using $P = P_0 \exp(-h/h_s)$, where P is atmospheric pressure, h is altitude, and P_0 and h_s are parameters. The parameter values were obtained by a fit to the altitude and pressure data below 13 hPa (fitted with 0.4% residual). The event rate gradually decreased with decreasing residual atmospheric pressure. Figure 30 shows the event rate as a function of atmospheric depth. The event rate grew linearly with atmospheric depth. This behavior is reasonable as atmospheric γ-rays.
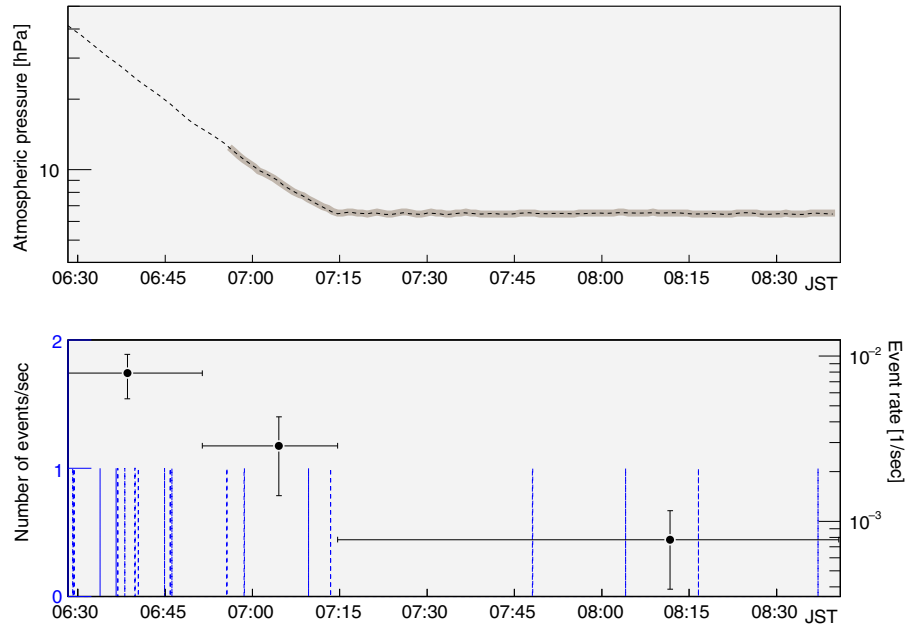
Fig. 29. The top graph shows the time profile of residual atmospheric pressure. Solid line (gray) corresponds to the pressure meter data. Dashed line (black) indicates residual atmospheric pressure converted from altitude with GPS. The bottom graph shows the time profile of γ-ray events. The histogram with the dashed line (blue) corresponds to the left axis. The points with error bars correspond to the right axis.

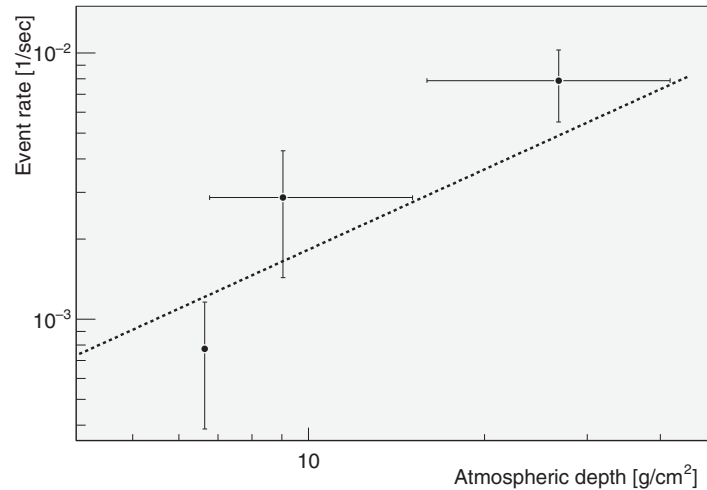**Fig. 30.** Event rate as a function of atmospheric depth. Dashed line shows linear fit with zero intercept.

We derived the atmospheric γ-ray flux. γ-ray events were used within a $30°$ zenith angle, excluding the Yorimodoshi-motor[5] angle region. In the Yorimodoshi-motor angle region, an excess of charged particle flux at level flight was seen due to the massive region. Thus we removed the γ-ray events in the Yorimodoshi-motor angle region. To correct for the detection efficiency, an efficiency map was created as a function of energy and incident zenith angle. The evaluation of the detection efficiency was described in Sect. 4.6. For the events with the lower limit of γ-ray energy, the energy was assumed

---

[5] The Yorimodoshi-motor was mounted on the upper part of the gondola by another group as a piggyback.
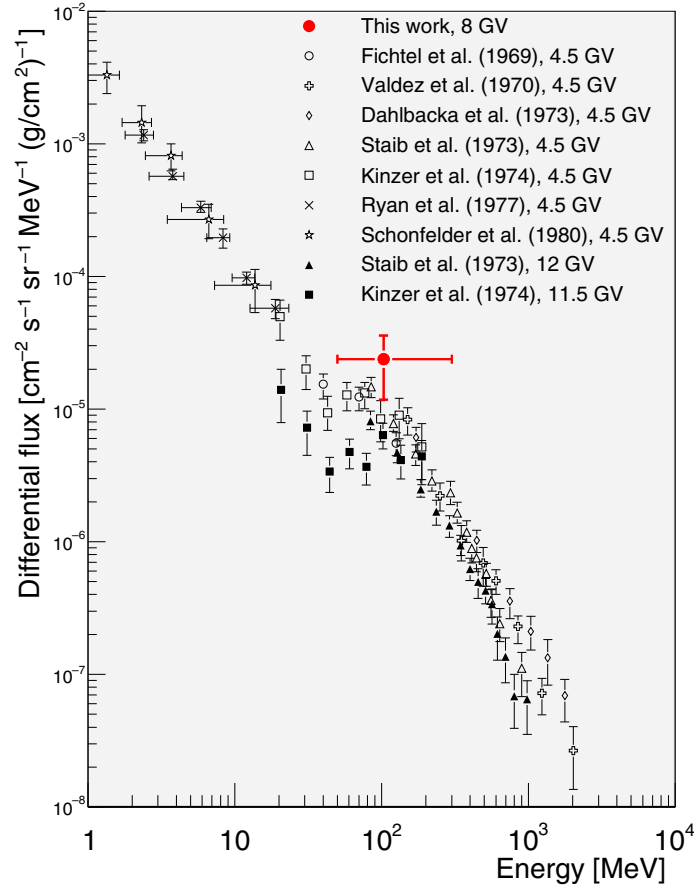
Fig. 31. Atmospheric γ-ray flux (see Refs. [34–40]).

from the opening angle of the electron pair. The timestamp efficiency was evaluated from the flight data for γ-ray energy and the incident zenith angle, as described in Sect. 4.7.

Figure 31 shows the derived atmospheric γ-ray flux compared with past measurements [34–40]. We measured the γ-ray flux in the range 50–300 MeV and our result was of a comparable level to past measurements. More precise measurement could be performed by expanding the analysis volume.

4.10.   *Determination of γ-ray arrival direction in celestial coordinates*

To determine the γ-ray arrival direction in celestial coordinates, γ-ray events were combined with attitude monitoring data. The attitude monitoring was performed by a star camera. The angle between the converter axis and the star camera axis was mechanically aligned with $\sim0.1°$ accuracy. This could be improved by data analysis from the relation between the incident γ-ray angle for the converter and the γ-ray elongation for the center of the γ-ray source position. The star camera worked at the level flight in daytime with an attitude determination ratio of 74%.

The inefficiency was due to a blanked-out periphery of the field of view ($\sim30\%$) by the front edge of the star camera hood and due to several periods without any detected stars. The attitude determination ratio could be improved by modifying the hood aperture and/or length, by selecting a camera with higher quantum efficiency (especially at longer wavelengths), and by setting multi-direction star cameras. The attitude monitoring was performed with a sufficient accuracy of $0.005°$ in elevation and $0.006°$ in azimuth.
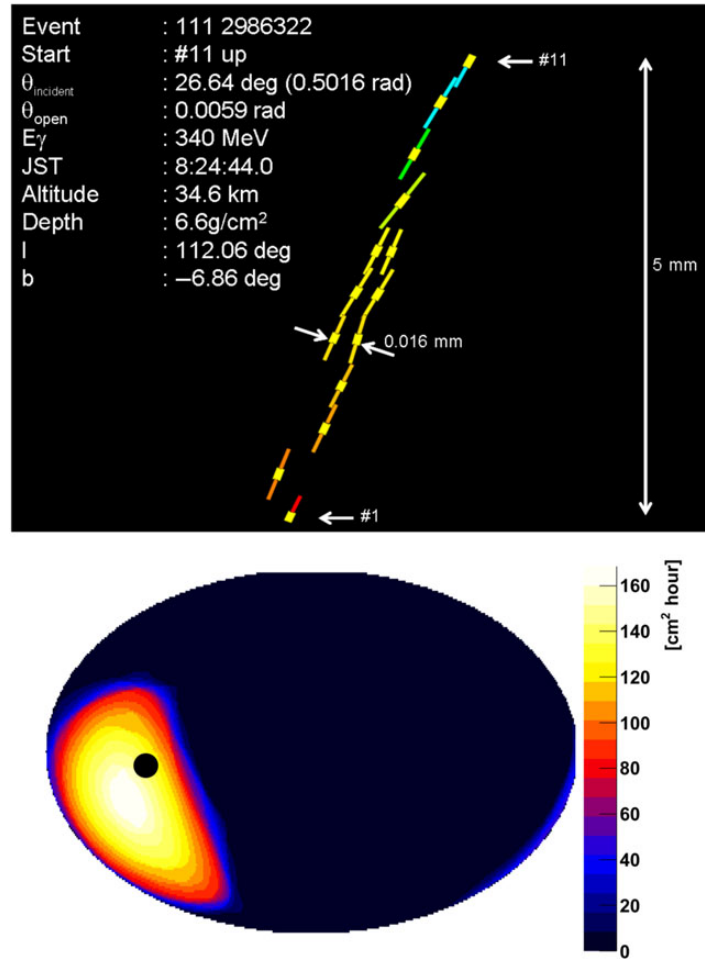
Fig. 32. Top figure shows the first light event. Bottom figure shows the sky map with Aitoff projection in galactic coordinates. The color bar shows the exposure (cm² hour) in this flight. A point (black) shows the position of the first light event.

The largest contribution to the attitude variation was rotation of the balloon gondola during the flight. The rotation velocity was measured with an absolute value of $<0.15°$/sec at 95% containment. By combining the 0.2 sec γ-ray timing resolution, an attitude determination was achieved with a sufficient accuracy of $<0.03°$ compared with the γ-ray angular resolution (Fig. 27). More details of the star camera and its flight data have been described elsewhere [41]. By combining attitude data, the γ-ray arrival direction was determined in celestial coordinates (Fig. 32). We established a procedure of γ-ray event detection, timestamping, and attitude combining, and performed the first light of the emulsion γ-ray telescope.

5.   Summary and outlook

We successfully performed a γ-ray observation balloon experiment with a $12.5 \times 10 \, \text{cm}^2$ aperture area and 4.6 hour flight duration in 2011.

Emulsion tracks were read across the whole area of the emulsion films and up to 45° for each projection angle in absolute values ($|\tan\theta_{\text{proj}}| < 1.0$). The readout tracks were reconstructed across the whole area of the emulsion films, up to 45° for each projection angle in absolute values

($|\tan\theta_{\rm proj}| < 1.0$) and down to 25 MeV/$c$ track momentum. Fine connection accuracy and uniform track efficiency were obtained across the whole area of the emulsion films.

We performed systematic detection of γ-ray events across the whole area of the emulsion film, up to 45° for each projection angle in absolute values ($|\tan\theta_{\rm proj}| < 1.0$), down to 50 MeV γ-ray energy and with 97% reliability. A systematic energy reconstruction was performed. The detected γ-ray events were timestamped with 0.2 sec timing accuracy and 98% timestamp reliability. Using the position, angle, and timing, we discriminated γ-rays produced in the converter. The discrimination not only allows suppression of the background, but could also be useful as a γ-ray calibration source (direction, timing, energy, polarization, and detection efficiency). We achieved high angular resolution and sufficient timing resolution with the flight data. We created a check and calibration method for the γ-ray data using the flight data.

We measured atmospheric γ-rays with our detector by a balloon flight. The derived flux was of a comparable level to past measurements. The atmospheric γ-rays can be explained as being the main background of cosmic γ-ray observations with emulsion telescopes by balloon flight. We obtained the first understanding of this background.

We measured the γ-ray flux in the energy range 50–300 MeV. This range includes an enhanced γ-ray emission feature from neutral pion (π^0) decay. Thus, this range is important for studying the γ-ray emission mechanism. γ-ray energy spectra of supernova remnants (SNRs), IC443 and W44, were measured down to 60 MeV with Fermi-LAT and detection of the π^0 feature was claimed [42]. These measurements are important for obtaining direct evidence that cosmic-ray protons are accelerated in SNRs. Current measurements have large systematic errors in the energy range of the enhanced π^0 feature due to the uncertainty of galactic diffuse emission. An emulsion telescope can achieve $\sim$10 times higher angular resolution compared with Fermi-LAT. Thus, an emulsion telescope can measure an energy spectrum with $\sim$100 times lower contamination of galactic diffuse emission. More precise measurement of the W44 energy spectrum in the energy range of the enhanced π^0 feature could be performed on the scale of $\sim$25 m^2 day (aperture area $\times$ flight duration of the emulsion telescope, e.g., 10 m^2 aperture area and 2.5 day flight duration (corresponding to 15 hours in the field of view)). Precise measurement can be performed not only for W44, but for other SNRs. A systematic study will be performed for cosmic-ray protons accelerated in SNRs. Precise measurements at low energies ($<\sim$70 MeV) may reveal new components. If electron-induced components appear, the first direct measurement of a high-energy proton–electron ratio in SNRs may be performed. By further exposure, a morphological study of SNRs could also be performed with high-resolution imaging. The advantage of the emulsion telescope is not only in cosmic-ray study, but also high-energy astrophysics, e.g., the study of the emission mechanism for pulsars, active galactic nuclei (AGNs), and gamma-ray bursts (GRBs) with polarization observations; and fundamental physics, e.g., searching for γ-rays from the annihilation/decay of dark matter at the galactic center with high-resolution imaging and the strictest verification of CPT invariance using distant sources (e.g., AGNs, GRBs) with polarization observations.

We established a procedure for determining the γ-ray arrival direction in celestial coordinates, detecting γ-ray events, timestamping, and combining attitude data. We performed the first light of the emulsion γ-ray telescope. The proposed emulsion telescope is feasible as a high-performance γ-ray telescope.

As a next step, we are planning a balloon experiment of CSIRO-JAXA international scientific ballooning at Alice Springs, Australia, with a 3600 cm^2 aperture area and $\sim$1 day flight duration. Figure 33 shows the multi-stage shifter intended for the next flight. In the next balloon experiment, we
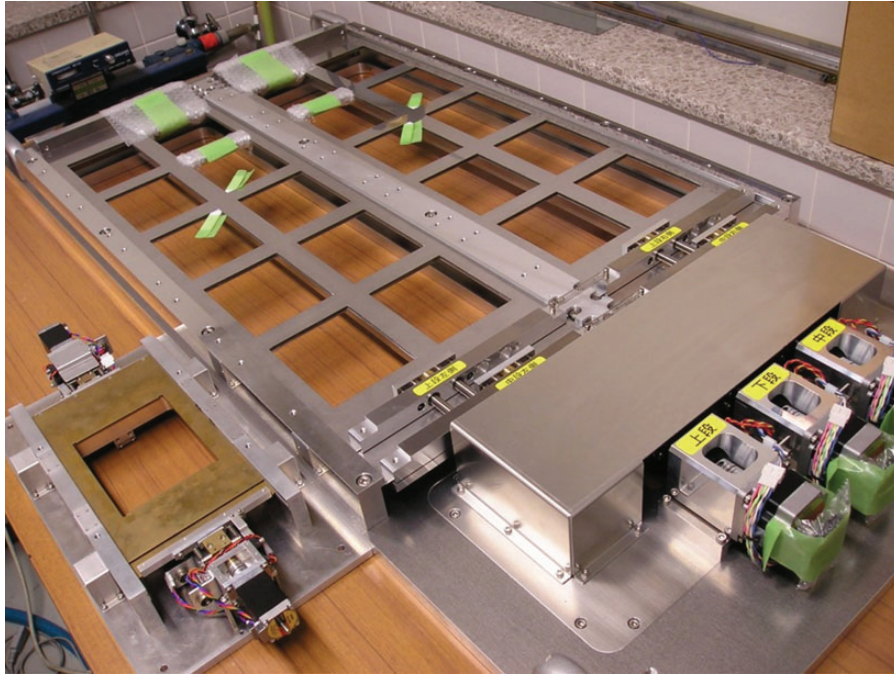
Fig. 33. Flight models of the multi-stage shifter. The left side shows the flight model used in the 2011 balloon experiment. The right side shows the next flight model. The next flight model has 3600 cm^2 aperture area. The flight models were co-developed with Mitaka Kohki Co., Ltd.

aim to observe the Vela pulsar, a well known bright γ-ray source, with more than 5σ significance and to demonstrate the overall performance of the emulsion telescope. Then, we will start the observation with the highest imaging resolution and polarization sensitivity; phase resolving of the pulse emission from the Vela pulsar will also be challenged.

We are pursuing various improvements for the next balloon experiment based on the experience and achievements of the 2011 balloon experiment. These experiments have the potential to expand our knowledge of high-energy phenomena in the universe.

References

[1] M. Tavani et al., Astron. Astrophys. **502**, 995 (2009).
[2] W. B. Atwood et al., Astrophys. J. **697**, 1071 (2009).
[3] P. L. Nolan et al., Astrophys. J. Suppl. **199**, 31 (2012).
[4] C. M. G. Lattes, H. Muirhead, G. P. S. Occhialini, and C. F. Powell, Nature **159**, 694 (1947).
[5] K. Niu, E. Mikumo, and Y. Maeda, Prog. Theor. Phys. **46**, 1644 (1971).
[6] K. Kodama et al., Phys. Lett. B **504**, 218 (2001).
[7] N. Agafonova et al., Phys. Lett. B **691**, 138 (2010).
[8] N. Agafonova et al., J. High Energy Phys. **11**, 036 (2013).
[9] N. Agafonova et al., Phys. Rev. D **89**, 051102(R) (2014).

[10] N. Agafonova et al., Prog. Theor. Exp. Phys. **2014**, 101C01 (2014).
[11] T. Nakamura et al., Nucl. Instrum. Meth. A **556**, 80 (2006).
[12] K. Hoshino et al., Proc. Int. Cosmic Ray Symp. on High Energy Phenomena, p. 149 (1974).
[13] S. Aoki et al., Nucl. Instrum. Meth. B **51**, 466 (1990).
[14] T. Nakano, *Automatic analysis of nuclear emulsion*, Ph.D. Thesis, Nagoya University, Japan (1997) [in Japanese].
[15] T. Nakano and K. Morishima, J. SPSTJ. **71**, 229 (2008).
[16] K. Morishima and T. Nakano, J. Instrum. **5**, P04011 (2010).
[17] S. Takahashi et al., Nucl. Instrum. Meth. A **620**, 192 (2010).
[18] S. Aoki et al., Adv. Space Res. **37**, 2120 (2006).
[19] S. Aoki et al., [arXiv:1202.2529] [Search ɪɴSPIRE].
[20] S. Aoki et al., Proc. 29th Int. Symp. on Space Technology and Science, 2013-m-02 (2013).
[21] S. Takahashi et al.,Proc. 33rd Int. Cosmic Ray Conference, p. 228 (2013).
[22] S. Takahashi, *Development of cosmic gamma-ray telescope with nuclear emulsion*, Ph.D. Thesis, Nagoya University, Japan (2011) [in Japanese].
[23] K. Ozaki, *Research for the Project of the Cosmic Gamma-Ray Observation with Nuclear Emulsion Telescope: Development of the attitude monitor/Study of the polarization detectability of linearly polarized gamma-ray with the nuclear emulsion*, Master Thesis, Kobe University, Japan (2012) [in Japanese].
[24] H. Fuke et al., Adv. Space Res. **45**, 490 (2010).
[25] H. Fuke et al., Adv. Space Res. **53**, 1432 (2014).
[26] N. Naganawa, and K. Kuwabara, Abstracts for SPIJ's Fall Conference in 2010, pp. 10–11 [in Japanese].
[27] H. Rokujo et al., Nucl. Instrum. Meth. A **701**, 127 (2013).
[28] N. Nonaka, *Development of NETSCAN method for nuclear emulsion and study*, Ph.D. Thesis, Nagoya University, Japan (2002) [in Japanese].
[29] K. Kodama et al., Nucl. Instrum. Meth. A **493**, 45 (2002).
[30] K. Hamada et al., J. Instrum. **7**, P07001 (2012).
[31] K. Kodama et al., Nucl. Instrum. Meth. A **574**, 192 (2007).
[32] S. Agostinelli et al., Nucl. Instrum. Meth. A **506**, 250 (2003).
[33] M. Ackermann et al., Astrophys. J. Suppl. **203**, 4 (2012).
[34] C. E. Fichtel, D. A. Kniffen, and H. B. Ogelman, Astrophys. J. **158**, 193 (1969).
[35] J. V. Valdez, P. S. Freier, and C. J. Waddington, Acta Phys. Suppl. **29**, 79 (1970).
[36] G. H. Dahlbacka, P. S. Freier, and C. J. Waddington, Astrophys. J. **180**, 371 (1973).
[37] J. Staib, G. Frye, and A. Zych, Proc. 13th Int. Conf. Cosmic Rays, p. 916 (1973).
[38] R. L. Kinzer, G. H. Share, and N. Seeman, J. Geophys. Res. **79**, 4567 (1974).
[39] J. M. Ryan, S. H. Moon, R. B. Wilson, A. D. Zych, R. S. White, and B. Dayton, J. Geophys. Res. **82**, 3593 (1977).
[40] V. Schonfelder, F. Graml, and F. P. Penningsfeld, Astrophys. J. **240**, 350 (1980).
[41] K. Ozaki et al., Proc. Balloon Symp., ISAS/JAXA, isas11-sbs-019 (2011) [in Japanese]. K. Ozaki et al., Proc. Balloon Symp., ISAS/JAXA, isas12-sbs-022 (2012) [in Japanese].
[42] M. Ackermann et al., Science **339**, 807 (2013).